The Astrophysical Journal, 985:198 (15pp), 2025 June 1 https://doi.org/10.3847/1538-4357/adccc0

Large Cold Dust Reservoir Revealed in Transitional SN Ib 2014C by James Webb Space Telescope Mid-infrared Spectroscopy

Samaporn Tinyanont[1], Ori D. Fox[2], Melissa Shahbandeh[2], Tea Temim[3], Robert Williams[2], Kittipong Wangnok[1,4], Armin Rest[2,5], Ryan M. Lau[6], Keiichi Maeda[7], Jacob E. Jencson[8], Katie Auchettl[9,10], Alexei V. Filippenko[11], Conor Larison[12], Chris Ashall[13], Thomas G. Brink[11], Kyle W. Davis[9], Luc Dessart[14], Ryan J. Foley[9], Lluís Galbany[15,16], Matthew Grayling[17], Joel Johansson[18], Mansi M. Kasliwal[19], Zachary G. Lane[20], Natalie LeBaron[11], Dan Milisavljevic[21], Jeonghee Rho[22], Itsuki Sakon[23], Arkaprabha Sarangi[24,25], Tamás Szalai[26,27], Kirsty Taggart[9], Schuyler D. Van Dyk[8], Qinan Wang[28,29], Yi Yang[11,30], WeiKang Zheng[11,31], and Szanna Zsíros[26]
[1] National Astronomical Research Institute of Thailand, 260 Moo 4, Donkaew, Maerim, Chiang Mai, 50180, Thailand; samaporn@narit.or.th
[2] Space Telescope Science Institute, Baltimore, MD 21218, USA
[3] Department of Astrophysical Sciences, Princeton University, 4 Ivy Lane, Princeton, NJ 08544, USA
[4] School of Physics, Institute of Science, Suranaree University of Technology, Nakhon Ratchasima, 30000, Thailand
[5] Department of Physics and Astronomy, The Johns Hopkins University, Baltimore, MD 21218, USA
[6] NSF's NOIRLab, 950 N. Cherry Ave., Tucson, AZ 85719, USA
[7] Department of Astronomy, Kyoto University, Kitashirakawa-Oiwake-cho, Sakyo-ku, Kyoto 606-8502, Japan
[8] IPAC, California Institute of Technology, 1200 E. California Blvd., Pasadena, CA 91125, USA
[9] Department of Astronomy and Astrophysics, University of California, Santa Cruz, CA 95064, USA
[10] School of Physics, University of Melbourne, VIC 3010, Australia
[11] Department of Astronomy, University of California, Berkeley, CA 94720-3411, USA
[12] Department of Physics & Astronomy, Rutgers, State University of New Jersey, 136 Frelinghuysen Road, Piscataway, NJ 08854, USA
[13] Institute for Astronomy, University of Hawai'i at Manoa, 2680 Woodlawn Dr., Hawai'i, HI 96822, USA
[14] Institut d'Astrophysique de Paris, CNRS-Sorbonne Université, 98 bis boulevard Arago, F-75014 Paris, France
[15] Institute of Space Sciences (ICE, CSIC), Campus UAB, Carrer de Can Magrans, s/n, E-08193 Barcelona, Spain
[16] Institut d'Estudis Espacials de Catalunya (IEEC), 08860 Castelldefels (Barcelona), Spain
[17] Institute of Astronomy and Kavli Institute for Cosmology, University of Cambridge, Madingley Road, Cambridge CB3 0HA, UK
[18] Oskar Klein Centre, Department of Physics, Stockholm University, SE-10691 Stockholm, Sweden
[19] Division of Physics, Mathematics, and Astronomy, California Institute of Technology, Pasadena, CA 91125, USA
[20] School of Physical and Chemical Sciences—Te Kura Matū, University of Canterbury, Private Bag 4800, Christchurch 8140, New Zealand
[21] Department of Physics and Astronomy, Purdue University, 525 Northwestern Ave., West Lafayette, IN 47907, USA
[22] SETI Institute, 189 Bernardo Ave., Ste. 200, Mountain View, CA 94043, USA
[23] Department of Astronomy, Graduate Schools of Science, University of Tokyo, 7-3-1 Hongo, Bunkyo-ku, Tokyo 113-0033, Japan
[24] Indian Institute of Astrophysics, Bengaluru 560034, India
[25] DARK, Niels Bohr Institute, Copenhagen, Denmark
[26] Department of Experimental Physics, Institute of Physics, University of Szeged, Dóm tér 9, 6720 Szeged, Hungary
[27] MTA-ELTE Lendület "Momentum" Milky Way Research Group, Szent Imre H. st. 112, 9700 Szombathely, Hungary
[28] Department of Physics and Kavli Institute for Astrophysics and Space Research, Massachusetts Institute of Technology, 77 Massachusetts Ave., Cambridge, MA 02139, USA
[29] TESS-ULTRASAT Joint Postdoctoral Fellow
[30] Physics Department, Tsinghua University, Beijing, 100084, People's Republic of China
[31] Bengier-Winslow-Eustace Specialist in Astronomy
Received 2025 February 19; revised 2025 April 3; accepted 2025 April 13; published 2025 May 23

Abstract

Supernova (SN) 2014C is a rare transitional event that exploded as a hydrogen-poor, helium-rich Type Ib SN and subsequently interacted with a hydrogen-rich circumstellar medium (CSM) a few months postexplosion. This unique interacting object provides an opportunity to probe the mass-loss history of a stripped-envelope SN progenitor. Using the James Webb Space Telescope (JWST), we observed SN 2014C with the Mid-Infrared Instrument Medium Resolution Spectrometer at 3477 days postexplosion (rest frame), and the Near-Infrared Spectrograph Integral Field Unit at 3568 days postexplosion, covering 1.7–25 μm. The bolometric luminosity indicates that the SN is still interacting with the same CSM that was observed with the Spitzer Space Telescope 40–1920 days postexplosion. JWST spectra and near-contemporaneous optical and near-infrared spectra show strong [Ne II] 12.831 μm, He 1.083 μm, Hα, and forbidden oxygen ([O I] $\lambda\lambda$6300, 6364, [O II] $\lambda\lambda$7319, 7330, and [O III] $\lambda\lambda$4959, 5007) emission lines with asymmetric profiles, suggesting a highly asymmetric CSM. The mid-IR continuum can be explained by $\sim$0.036 $M_\odot$ of carbonaceous dust at $\sim$300 K and $\sim$0.043 $M_\odot$ of silicate dust at $\sim$200 K. The observed dust mass has increased tenfold since the last Spitzer observation 4 yr ago, with evidence suggesting that new grains have condensed in the cold dense shell between the forward and reverse shocks. This dust mass places SN 2014C among the dustiest SNe in the mid-IR and supports the emerging observational trend that SN explosions produce enough dust to explain the observed dust mass at high redshifts.

Unified Astronomy Thesaurus concepts: Core-collapse supernovae (304); Type Ib supernovae (1729); Dust formation (2269)

1. Introduction

Mass loss dictates the evolution of massive stars ($\gtrsim$8 $M_{\odot}$) and their eventual deaths as core-collapse supernovae (CCSNe). For about a third of all CCSNe (e.g., N. Smith et al. 2011b; I. Shivvers et al. 2017), the progenitor star loses its hydrogen (Type Ib) or even helium (Type Ic) envelopes and explodes as a stripped-envelope supernova (SESN; for review, see, e.g., A. V. Filippenko 1997; A. Gal-Yam 2017). For about 10% of CCSNe (N. Smith et al. 2011b; I. Shivvers et al. 2017), mass loss concludes soon before, or is still ongoing, at the time of core collapse, leaving a nearby dense circumstellar medium (CSM). The supernova (SN) shock interacts with this CSM, heating the material and producing light, resulting in luminous interacting SNe with relatively narrow ($\sim$100–1000 km s^{-1}) emission lines from hydrogen (Type IIn; E. M. Schlegel 1990), helium (Type Ibn; A. Pastorello et al. 2008), or heavier elements (Type Icn; A. Gal-Yam et al. 2021; C. Pellegrino et al. 2022). By observing these interacting SNe, we can reconstruct the CSM structure and the mass-loss history as the SN shock sweeps out and interacts with older material. Critically, emission from interacting SNe emerges in the infrared (IR) at late times as the interaction flux gets absorbed, thermalized, and reemitted by dust, either preexisting or newly formed. Therefore, late-time observations in the IR reveal the nature of the mass-loss process responsible for the diversity of the CCSN population.

Observations in the past decade provide evidence that binary interaction (P. Podsiadlowski et al. 1992) is the primary mechanism for producing the majority of SESN progenitors (J. J. Eldridge et al. 2013; see reviews by N. Smith 2014, 2017). First, single-star wind-driven mass loss (even assuming high mass-loss rate classical wind prescriptions; e.g., C. de Jager et al. 1988) cannot explain the relatively large SESN fraction, as only the most massive CCSN progenitors could completely lose all of their hydrogen this way. Empirical measurements of mass-loss rates for massive stars have also shown that the classic prescriptions overestimate the mass-loss rate by a factor of $\sim$20 (E. R. Beasor & B. Davies 2018; E. R. Beasor et al. 2020), further limiting the prospect of stripping a star in this manner (E. R. Beasor & N. Smith 2022). Second, the majority of massive stars capable of producing CCSNe live in close-in binary systems, in which mass transfer is expected (H. Sana et al. 2012). Binary mass-transfer can strip lower-mass stars and could explain the high rate of SESNe (N. Smith et al. 2011b; I. Shivvers et al. 2017) and their typically low ejecta mass (M. R. Drout et al. 2011; J. D. Lyman et al. 2016). Recently, a population of stripped intermediate-mass helium stars thought to be produced by this process has been identified in the Magellanic Clouds (M. R. Drout et al. 2023). Environmental studies of SESN sites point to generally intermediate age ($\sim$10 Myr), inconsistent with the very young age ($\sim$1 Myr) expected if they come from very massive stars (e.g., L. Galbany et al. 2018; H. Kuncarayakti et al. 2018; N. C. Sun et al. 2020, 2023), further suggesting that most SESNe come from lower-mass progenitors. Most recently, direct imaging with Hubble Space Telescope (HST) has detected putative surviving companion stars at the positions of several nearby SESNe, further supporting the binary scenario (E. Zapartas et al. 2017; S. D. Ryder et al. 2018; O. D. Fox et al. 2022, and references therein).

To measure the mass-loss rate and CSM profile and further support the binary origin of SESNe, we need to directly observe events with CSM interaction. Unlike other interacting SNe that start interacting immediately after the explosion, we expect CSM around SESNe to be at some distance from the progenitor; the stripped star is expected to live for some time after the conclusion of the binary mass-transfer process. As such, the interaction could begin months to years after the explosion, or not at all if the delay is too great and the CSM has already been dispersed by the time the progenitor dies. To detect these late CSM interactions, observations in the IR are key as the spectral energy distribution (SED) of the SN shifts red owing to newly formed or preexisting dust.

Massive stellar systems experiencing mass loss before undergoing a SESN, as well as interacting SN progenitors, have conditions suitable for dust production. Dust has been observed in Galactic post-binary-interaction systems, which are thought to be SESN progenitor candidates, such as RY Scuti (R. D. Gehrz et al. 1995; N. Smith et al. 2011a) and NaSt1 (J. Mauerhan et al. 2015). Other extreme massive Galactic stars thought to resemble interacting SN progenitors, such as luminous blue variables, also harbor dusty CSM (L. B. F. M. Waters et al. 1998; C. Agliozzo et al. 2021). In addition, large quantities of dust are present in interacting SNe, reprocessing the interaction flux and making them especially luminous and long lasting in the IR (O. D. Fox et al. 2011, 2013; S. Tinyanont et al. 2016; T. Szalai et al. 2019). Consequently, the IR dominates the SED of these transients at late times. Thus, IR observations of interacting SNe months to years after explosion are crucial for (1) probing the presence of detached CSM around SESNe, and (2) determining whether the CSM dust can survive the shock passage, or reform behind the shock, and be dispersed into the interstellar medium.

We have discovered at least eight SESNe, listed below, that show late-time rebrightening and spectroscopic evolution consistent with a delayed interaction with detached hydrogen-rich CSM from the lost stellar envelope. Members of this class include SNe 2001em (N. N. Chugai & R. A. Chevalier 2006; P. Chandra et al. 2020), 2004dk (J. C. Mauerhan et al. 2018; D. Pooley et al. 2019; A. Balasubramanian et al. 2021), 2014C (D. Milisavljevic et al. 2015; R. Margutti et al. 2017), and more recently SNe 2018ijp (L. Tartaglia et al. 2021), 2019oys (J. Sollerman et al. 2020), and 2019yvr (C. D. Kilpatrick et al. 2021; L. Ferrari et al. 2024). Some objects, like SN 2019tsf (J. Sollerman et al. 2020; Y. Zenati et al. 2022) and SN 2022xxf (H. Kuncarayakti et al. 2023), have shown rebrightening and radio emission without hydrogen or helium lines, which have been attributed to interactions with hydrogen-free and helium-poor CSM. In addition, there are SESNe with interactions inferred from archival IR photometry from the Wide-field Infrared Survey Explorer (C. Myers et al. 2024). Among this emerging class of interacting SESNe, the most well-observed member remains SN 2014C.

SN 2014C was first discovered on 2014 January 5 (UTC dates are used throughout this paper; W. Zheng et al. 2014) in NGC 7331. We adopt the Cepheid distance of 14.7 $\pm$ 0.6 Mpc to the host galaxy (W. L. Freedman et al. 2001). The recent photometric analysis by Q. Zhai et al. (2025) puts the explosion date on 2014 January 1 (MJD 56658.91). However, we keep January 5 as our reference epoch to be consistent with S. Tinyanont et al. (2019), as the difference of 4 days is insignificant at our epoch of observation. The SN was quickly classified as a hydrogen-poor Type Ib SN (M. Kim et al. 2014). After a few months in solar conjunction, it reemerged and was observed on 2014 April 20, 105 days postexplosion with growing narrow- and intermediate-width hydrogen emission

lines (Q. Zhai et al. 2025), marking a transition from Type Ib to Type IIn. The shocked CSM produced strong radio and X-ray emission (R. Margutti et al. 2017). These data highlighted an interaction between the SN shock and the hydrogen-rich envelope lost from the progenitor star. R. Margutti et al. (2017) presented archival radio observations and showed that SN 2014C-like interaction was observed in ∼10% of SESNe. Recent optical data published by Q. Zhai et al. (2025) suggest that weaker interaction may have commenced as early as 20 days postexplosion.

Early time observations, particularly at X-ray wavelengths, reveal that SN 2014C has a dense, uniform CSM shell with $\sim 1\,M_{\odot}$ at about 5×10^{16} cm (3000 au) away from the star (R. Margutti et al. 2017). More recently, J. C. Mauerhan et al. (2018), B. P. Thomas et al. (2022), and D. Brethauer et al. (2022) presented long-term observations of SN 2014C in the optical and X-rays. Their key finding is that the CSM must be asymmetric, with high-density regions required to explain different line widths observed in Hα and various metal lines, and the low density inferred from X-ray observations. In addition, very-long-baseline interferometry (VLBI) of SN 2014C spatially resolved the forward shock, showing minimal deceleration and an asymmetric shape (M. F. Bietenholz et al. 2018, 2021). These observations point to a toroidal CSM around SN 2014C, and recent theoretical 3D simulation work by S. Orlando et al. (2024) supports this interpretation.

To accurately measure the density profile of the CSM around SN 2014C, we needed to measure its bolometric luminosity evolution, which required observations near the peak of the SED in the IR. SN 2014C was monitored in the IR from explosion to 1920 days postexplosion as part of the SPitzer InfraRed Intensive Transients Survey (S. Tinyanont et al. 2016; M. M. Kasliwal et al. 2017). S. Tinyanont et al. (2019) modeled the bolometric light curve with a semianalytic model of T. J. Moriya et al. (2013) and showed that the CSM has a $\rho \propto r^{-2}$ density profile with a large mass-loss rate of $\sim 10^{-3}\,M_{\odot}\,\mathrm{yr}^{-1}$, consistent with binary-induced mass loss. With a 10 μm detection from the ground, they also showed that silicate dust, about 30% by mass, must be present in the CSM of SN 2014C. The inferred dust mass, assuming the mixed carbonaceous and silicate composition, remained constant around $5 \times 10^{-3}\,M_{\odot}$ throughout the observations, indicating that the dust was preexisting. By the end of the Spitzer mission in 2020, SN 2014C remained a luminous IR source.

Here, we present James Webb Space Telescope (JWST) observations of SN 2014C 3477–3568 days postexplosion, along with ground-based optical and near-IR (NIR) spectroscopy from similar epochs. We describe the observations and data reduction in Section 2. The dust parameter fitting and bolometric luminosity are presented in Section 3. Section 4 discusses the evolution of spectral line profiles. Our conclusions are summarized in Section 5.

2. Observations and Data Reduction

2.1. JWST NIRSpec and MIRI MRS

SN 2014C was observed with JWST as part of program GO-2348 (PI Tinyanont) on 2023 July 25 (3477 days postexplosion, rest frame) using the Mid-InfraRed Instrument (MIRI) in the Medium Resolution Spectrometer (MRS; M. Wells et al. 2015; I. Argyriou et al. 2023), and on 2023 October 24 (3568 days postexplosion) using the Near-InfraRed Spectrograph (NIRSpec) in the integral-field unit (IFU) mode (P. Jakobsen et al. 2022; T. Böker et al. 2023).

We obtained MIRI MRS observations in all subbands to ensure the full wavelength coverage of 4.9–27.9 μm. We used a four-point dither pattern optimized for point sources to observe the SN. All exposures used the FASTR1 readout pattern with 30 groups per integration, 1 integration per exposure, and 1 exposure at each dithering point (4 total), yielding the total of 333 s exposure time for each subband. Dedicated background observations were also performed with the same exposure time but without dithering. We also obtained parallel MIRI imaging in the F560W, F1000W, and F1130W filters, covering the field adjacent to the SN.

The NIRSpec IFU observations were conducted with two filter/grating configurations, F170LP/G235H and F290LP/G395H, to cover 1.66–5.27 μm. Both observations used the four-point-nod dither and the NRSIRS2RAPID readout pattern. The F170LP/G235H and F290LP/G395H observation employed five and three groups per integration, respectively. Both observations used one integration, and one exposure at each dither point (four total), yielding 350 and 233 s total exposure times for the F170LP/G235H and F290LP/G395H setups, respectively. Owing to the expected brightness of the source, no "leakcal" observations to remove contamination from stuck-open shutters in the microshutter assembly were requested.

From the automatically reduced spectral cube provided on the Barbara A. Mikulski Archive for Space Telescopes (MAST), we note that the observations are offset from previous HST observations of the same field.[32] To improve the world coordinate system solution of the final data cube, we measure the coordinate offsets in our observations by the following procedure. First, we download an HST image of the field that covers the SN and has a significant overlap with the MIRI parallel images. We used the F555W image obtained with the Wide-Field Camera 3 (WFC3) on 2022 July 31 (PID 16691; PI Foley; this image along with the aligned MRS cube is shown in Figure 1, top right). We align it to the Gaia DR2 catalog using the JWST HST Alignment Tool (JHAT; A. Rest et al. 2023)[33] and produce a secondary catalog of sources from the deeper HST image. We then align the MIRI parallel image in the F560W band to this secondary catalog. We use the bluest MIRI image to ensure that there are enough common point sources between it and the optical image. Finally, we compute the R.A. and decl. offsets from this process, and apply the same offset to the coordinates in the MRS files.

We use the JWST data-reduction pipeline v1.15.1[34] to process the raw data with the Calibration Reference Data System v11.17.20.[35] For both NIRSpec and MIRI MRS, we download uncalibrated files from MAST and run the Stage 1 pipeline to fit the observed ramp and produce rate files. The reference coordinates for the rate files are updated by adding the R.A. and decl. offsets found using JHAT to the `RA_REF` and `DEC_REF` FITS header keywords of MRS observations. We run the `spec2` pipeline stage to generate calibrated files. At this stage, we remove the background from the telescope and the zodiacal light. We extract 1D background spectra from

[32] These data can be retrieved at doi:10.17909/adcj-n781.
[33] https://jhat.readthedocs.io/
[34] https://jwst-pipeline.readthedocs.io/
[35] https://jwst-crds.stsci.edu/

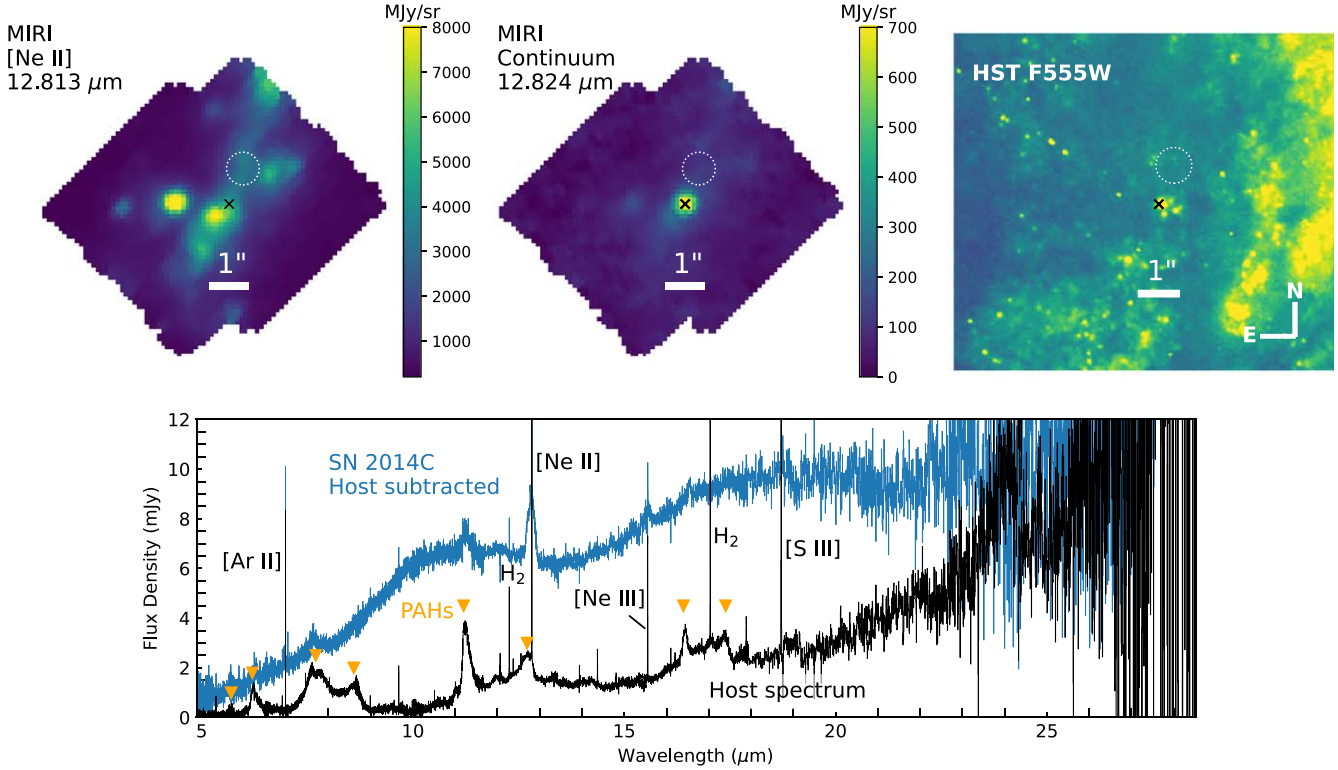

Figure 1. Top: images of SN 2014C from MIRI MRS slice at the rest wavelength of [Ne II] 12.813 μm (left), continuum at 12.824 μm (center), and HST/WFC3 F555W (right; PID 16691; PI Foley). The SN is marked with a cross. North is up, and east is to the left in all images. The HST image was used to align the MIRI parallel image, and applied to the MIRI MRS data. The [Ne II] 12.813 μm image is representative of the complex host environment around SN 2014C. We note that a broad [Ne II] line associated with the SN is detected in addition to the host emission. The contaminating flux is mostly in narrow lines, and does not affect our measurements. To estimate the continuum host emission, we use the circular aperture shown as a dashed white circle, which selects an area with emission similar to that at the SN location, and is far enough as to not self-subtract the SN at longer wavelengths (the SN flux in this background aperture is <1% in MRS Channel 4). Bottom: MRS spectrum of SN 2014C with the host emission (estimated from the aperture shown in the top figures) subtracted. The host spectrum used for subtraction is shown in black, in the same units as the SN spectrum. Strong narrow host lines are labeled, while PAHs bands at 5.7, 6.2, 7.7, 8.6, 11.2, 12.7, 16.4, and 17.4 μm are marked with orange triangles.

our dedicated background pointing using the `Extract1D` function with the source type set to `EXTENDED`. This way, the entire field of view is used, reducing the noise in the measurement. We then rerun the `spec2` pipeline using this extracted spectrum for master background subtraction.

After this step, we run the `spec3` pipeline stage to drizzle and combine the dithered, dedicated-background-subtracted observations, keeping different channels and bands separate. This results in 12 spectral cubes from MRS, from Channels 1 to 4, with the short, long, and medium bands per each channel.

2.2. Host Background Subtraction

While the thermal background from the sky and the telescope is removed using the dedicated background observations, the cubes still have a significant, spatially varying host-galaxy background underneath the SN. The pipeline provides a basic tool to measure and subtract background in an annulus around the source during spectral extraction, and the annulus size scales with the wavelength. However, with our spatially varying background, it is crucial to sample the background from the same region at all wavelengths. To do this, we place a circular aperture with a radius of 0.″52 at $\alpha = 22^{h}37^{m}05\overset{s}{.}57$, $\delta = +34°24'32\overset{''}{.}517$, shown in Figure 1 (top). This location is along the prominent elongated structure running northwest to southeast through the SN, and it is far enough away from the SN to include <1% of the SN light at the reddest wavelength according to the point-spread-function (PSF) model. It also avoids all the star-forming knots observed in strong lines (e.g., Figure 1, top left; other lines show star-forming knots at similar locations). At each wavelength slice in the spectral cubes, we subtract the surface brightness measured in this aperture from the whole slice.

Finally, we perform spectral extraction of the SN from the host-subtracted cubes using the `Extract1d` step in the JWST pipeline. Figure 1 (top) shows the final spectral cube from MRS compared with the HST image. The brightest source in the MRS cube is well aligned with the location of the SN from the HST/WFC3 F555W image from 2022 (PID 16691; PI Foley). We extract the 1D spectrum at this location from the host-subtracted cubes for further analysis. The JWST pipeline extracts 1D spectra for a point source by performing aperture photometry in each slice. We set the aperture size to be equal to the full width at half-maximum (FWHM) intensity of the PSF at that wavelength (by setting the parameter `ifu_rscale`=1.0). An aperture correction is then applied. We note that fluxes in the overlapping regions between different channels and bands agree with each other, and we do not apply further scaling. Figure 1 (bottom) shows the final SN spectrum along with the host background spectrum used for the subtraction. The strong, broad emission features from polycyclic aromatic hydrocarbons (PAHs) at (for example) 7.7, 11.3, and 16.4 μm, which are from the host galaxy and unlikely from the SN, have been mostly removed, demonstrating that the selected background aperture is appropriate. Figure 2 (left) compares this spectrum to the 2019 observations of SN 2014C

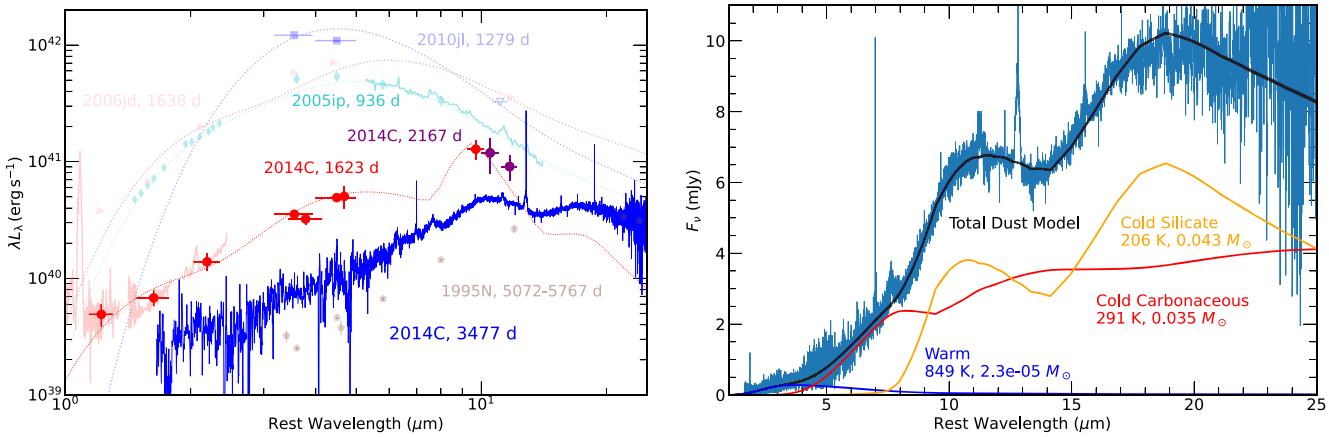

Figure 2. Left: NIR to mid-IR spectrum of SN 2014C from JWST NIRSpec IFU and MIRI MRS, from 3568 and 3477 days postexplosion, respectively. The IR spectra and photometry of SN 2014C at 1623 days published by S. Tinyanont et al. (2019), along with all mid-IR data of SNe IIn from before 2019 (also shown in Figure 6 of S. Tinyanont et al. 2019), are displayed for comparison. The ground-based mid-IR photometry from Subaru/COMICS at 2167 days postexplosion is also shown. The best dust model is shown for every SN, except SN 1995N, for which the spectrum resembles a power law. For SN 2014C, we note that the photometry at 2167 days deviates from the model fitted to the 1623 day SED. This is consistent with the SN cooling down in the 1.5 yr between the two observations. Right: mid-IR spectrum of SN 2014C with the best-fit dust model retrieved from MCMC fitting. The model requires three dust components, whose best-fit parameters are summarized in Table 1.

from S. Tinyanont et al. (2019) along with other objects in the literature.

2.3. Keck LRIS and NIRES Optical to NIR Spectroscopy

SN 2014C was observed with the Low-Resolution Imaging Spectrometer (LRIS; J. B. Oke et al. 1995) on the Keck I 10 m telescope on Maunakea, Hawaii, on 2022 August 2 (3121 days postexplosion), 2022 November 20 (3230 days), and 2024 June 3 (3789 days). The data were reduced using `LPipe` (D. A. Perley 2019). Flux calibration was performed using a spectrophotometric standard star observed on the same night. These new optical spectra are shown in Figure 3.

SN 2014C was observed with the Near-InfraRed Echellette Spectrometer (NIRES; J. C. Wilson et al. 2004) on the Keck II 10 m telescope on 2024 June 21 (3807 days postexplosion) as part of the Keck Infrared Transient Survey (S. Tinyanont et al. 2024). The observations were performed with two sets of the ABBA dithering pattern to sample the sky background, with a total exposure time of 2400 s. The A0 V star HIP111538 was observed immediately before the SN to provide flux and telluric calibration. We reduced the data using `pypeit` (J. Prochaska et al. 2020a; J. X. Prochaska et al. 2020b) following the procedure outlined by S. Tinyanont et al. (2024), automatically performing flat-fielding, background subtraction, and source detection and extraction. The science spectra were then flux calibrated, coadded, and corrected for telluric absorption, using the aforementioned A0 V star observation. Only the He I 1.083 μm was detected.

2.4. Subaru COMICS Mid-IR Photometry

SN 2014C was observed by the Cooled Mid-infrared Camera and Spectrometer (COMICS; H. Kataza et al. 2000) on the Subaru Telescope in the N10.5 ($\lambda_c = 10.5\,\mu$m, $\Delta\lambda = 1.0\,\mu$m) and N11.7 ($\lambda_c = 11.7\,\mu$m, $\Delta\lambda = 1.0\,\mu$m) filters on 2019 December 12, before the instrument was decommissioned. Individual 200 s exposures were taken in chopping-only mode with a chop amplitude of 10″; the total integration times on SN 2014C were 94 and 37 minutes for the N10.5 and N11.7 filters, respectively. 11 Lac (HR 8632) was used as the photometric standard star from the list of mid-IR standards given by M. Cohen et al. (1999). The measured fluxes were 16.1 ± 5.4 mJy and 13.7 ± 3.4 mJy in the N10.5 and N11.7 filters, respectively, and are shown in Figure 2 (left).

3. Dust Emission in the Mid-IR

3.1. Spectrum Fitting and Dust Parameter Estimation

We fit the IR spectrum of SN 2014C with a combination of dust models to determine the dust temperatures, masses, and compositions. The set of equations presented by M. Shahbandeh et al. (2023) is employed. The observed dust flux is given by

$$F_{\rm dust}(\lambda) = \frac{B(\lambda, T_{\rm dust})\kappa(\lambda)M_{\rm dust}P_{\rm esc}(\tau)}{d^2}, \quad (1)$$

where B is the Planck function, d is the distance to the SN, and κ is the dust opacity from B. T. Draine & H. M. Lee (1984) and A. Laor & B. T. Draine (1993) assuming a grain size of $a = 0.1\,\mu$m. We note that, in the IR, $\lambda \gg a$, and the spectral shape is insensitive to the grain size (e.g., O. D. Fox et al. 2010; A. Sarangi 2022). Large grains with $a > 1\,\mu$m are not expected in SNe at this phase, and they cannot reproduce the strong silicate feature observed. Per D. P. Cox & W. G. Mathews (1969), the escape probability $P_{\rm esc}(\tau)$, assuming spherical symmetry, is given by

$$P_{\rm esc}(\tau) = \frac{3}{4\tau}\left[1 - \frac{1}{2\tau^2} + \left(\frac{1}{\tau} + \frac{1}{2\tau^2}\right)e^{-2\tau}\right]. \quad (2)$$

The optical depth, assuming that the dust is evenly distributed inside the expanding SN, is

$$\tau(\lambda, t) = \rho(t)R(t)\kappa(\lambda) = \frac{3}{4}\frac{M_{\rm dust}(t)}{\pi R(t)^2}\kappa(\lambda). \quad (3)$$

We leave the radius R as a free parameter because the shock velocity at this phase is unclear. We note that a generic shock velocity of 10,000 km s^{-1} used by S. Tinyanont et al. (2019),

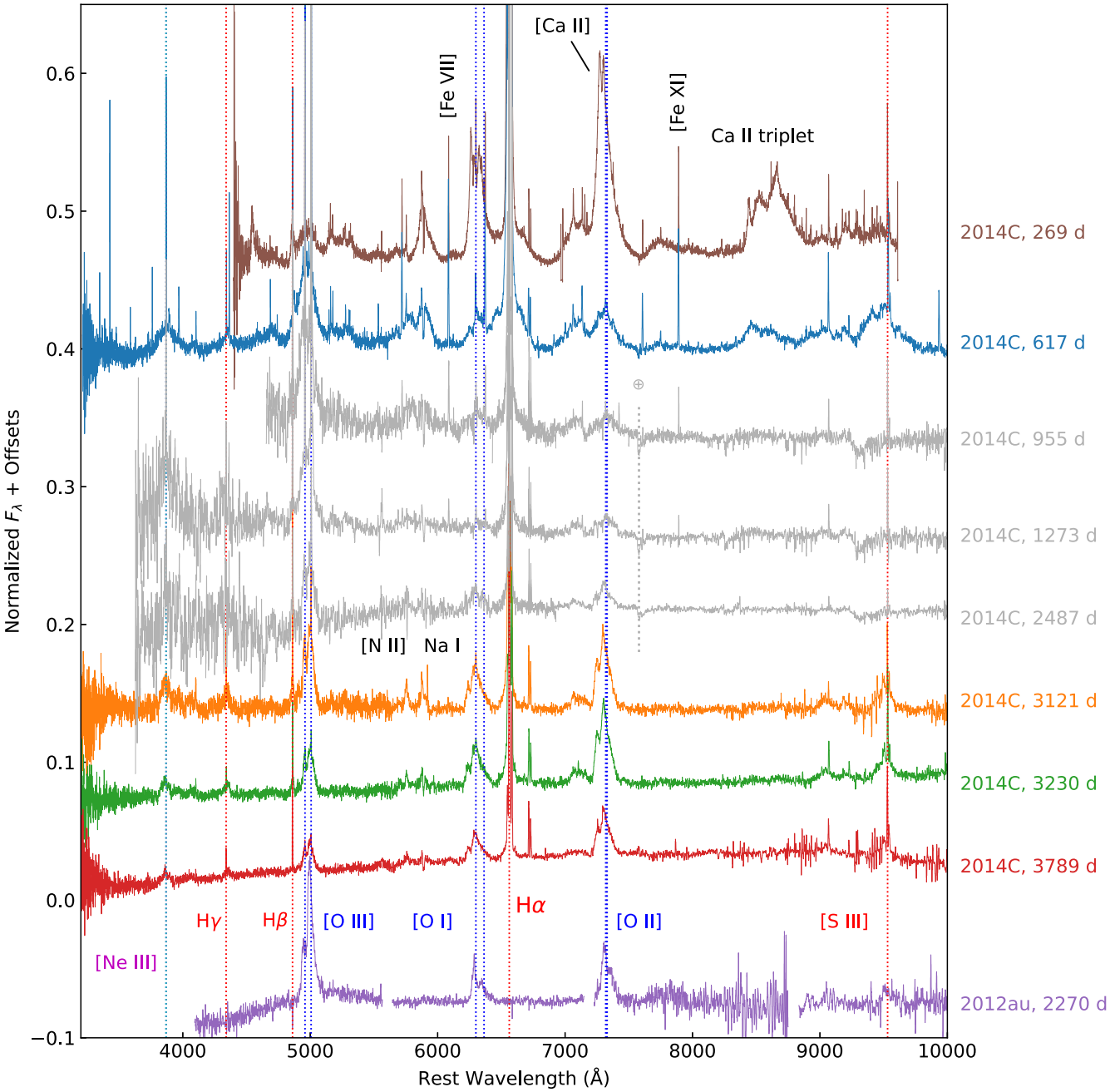

Figure 3. New optical spectra of SN 2014C from 3131, 3230, and 3789 days compared with earlier spectra from J. C. Mauerhan et al. (2018) at 269 and 619 days, and from B. P. Thomas et al. (2022) at 955, 1273, and 2487 days (note that we merge their red and blue spectra taken at similar time to cover a wider wavelength coverage and report the average epoch). The spectrum of SN 2012au at 2270 days from D. Milisavljevic et al. (2018) is provided for comparison.

consistent with early time spectroscopy (D. Milisavljevic et al. 2015; Q. Zhai et al. 2025), would result in $R = 3 \times 10^{17}$ cm at the epoch of the MRS observation.

Here, we note that the spherical geometry assumption does not significantly affect our results. Because both $M_{\rm dust}$ and R are free parameters, τ is effectively a free parameter as well, and the geometry is only used to compute the escape probability. As we will show, the optical depth in the IR is low at this epoch, and the assumed geometry here does not affect our results.

We first determine how many dust components are required to explain our data by performing a nonlinear least-squares minimization fit using the `curve_fit` routine from the `scipy.optimize` package. Each component has a unique temperature, mass, and composition (either carbonaceous or silicate, which have different opacity, but with a fixed grain size). The optical depth used in the fit is the total optical depth from all components considered. More components are added iteratively until a satisfactory fit is achieved. We find that three dust components are required; their properties, from the subsequent Markov Chain Monte Carlo (MCMC) fitting, are summarized in Table 1. The warm component with $T \approx 800$ K is needed to explain the NIR flux, while the majority of dust mass is found in the cold components. The broad spectral features observed at around 11 and 18 μm are indicative of a cold silicate dust component. Another cold carbonaceous component is needed to fit the overall flux in the mid-IR.

Table 1
Best-fit Dust Parameters for SN 2014C

Component	T (K)	M ($M_\odot$)	Composition
Warm	850 ± 4	$(2.30 \pm 0.05) \times 10^{-5}$	C
Cold C	291 ± 1	0.0355 ± 0.0005	C
Cold Si	207 ± 1	0.0425 ± 0.0003	Si
Total	245[a]	0.0780 ± 0.0006	

Note.
[a] Mass-averaged temperature. Uncertainties provided are statistical errors only. The mass uncertainty is dominated by the distance uncertainty to the SN.

To sample the posterior distribution of our fitted parameters, we perform an MCMC fit using `emcee` (D. Foreman-Mackey et al. 2013). We assume a flat prior distribution for all parameters within a physical range, and use the results from our preliminary least-squares minimization fit as initial values. Further details of the MCMC run can be found in the Appendix, and the results including 1σ uncertainties are summarized in Table 1. The mass uncertainty provided here only includes statistical uncertainty. A more representative uncertainty for dust mass is twice the distance uncertainty to the SN: about 8%. The best-fit radius (assuming spherical geometry) is $R = (3.82 \pm 0.06) \times 10^{17}$ cm. The best-fit model is shown over the data in Figure 2 (right).

The average best-fit optical depth of the cold silicate and carbonaceous dust components is $\tau \approx 0.15$ in the IR continuum. The symmetric posterior distribution (Figure A.1) of the dust masses also indicates that the dust is optically thin; otherwise, it would plateau toward high mass as the majority of the dust cloud is not visible. Here, we reiterate that, by leaving R as a free parameter, τ is effectively a free parameter as well, so the result is only dependent on the assumed geometry through the $P_{\rm esc}$ calculation.

The observed mid-IR spectrum of SN 2014C indicates that SN 2014C now harbors a total of $0.0780\,M_\odot$ of cold dust with a temperature of $\sim$245 K. A mixture of carbonaceous (46% by mass) and silicate (54%) dust is required to fit the observed spectral features. This is roughly consistent with the silicate dust mass fraction found previously by S. Tinyanont et al. (2019). From 2019 until 2023, the minimum dust mass required to fit the SED of SN 2014C has increased by more than an order of magnitude (Figure 4(b)), while the temperature has dropped from around 500 to 250 K (Figure 4(a)). Such an evolution points to new dust formation, which we discuss in more details in Section 3.3.

3.2. Bolometric Luminosity

The total luminosity of the SN at this epoch is key to determining its powering mechanism, almost 10 yr postexplosion. The SED of SN 2014C at the JWST epoch peaks in the mid-IR, around 20 μm. Therefore, we measure the bolometric luminosity by integrating the high signal-to-noise ratio (S/N) part of the observed spectrum between 2.5 and 22 μm, and adding the missing flux from the best-fit dust model discussed in the previous section. We determine the bolometric luminosity at 3477 days postexplosion to be $(6.5 \pm 0.2) \times 10^{40}$ erg s^{-1} (86% of which is observed with JWST and 14% is from extrapolation).

The bolometric luminosity from the JWST observations is shown in Figure 4(c), along with the bolometric light curve inferred from Spitzer observations (S. Tinyanont et al. 2019). The powering mechanism at this epoch is the CSM interactions that get reprocessed into the IR by dust. The semianalytic light curve of an SN interacting with a CSM with $\rho = Dr^{-2.01\pm0.01}$, where $D = 10^{14.9\pm0.2}$ g cm^{-1}, presented by S. Tinyanont et al. (2019; fit to only the Spitzer data), is plotted. The observed bolometric luminosity agrees well with the model prediction, indicating that the SN is still interacting with the same CSM component responsible for the light curve up to 1920 days postexplosion. The lack of extra luminosity, which would have been evidence for an additional denser CSM, rules out the possibility that the increased observed dust mass is more preexisting dust farther out from the SN.

Furthermore, we can compute the mass in the extended CSM that has interacted with the SN so far, using the CSM density profile from S. Tinyanont et al. (2019). Because of the wind-like $\rho \propto r^{-2}$ profile, the swept-up CSM mass is $M_{\rm CSM,wind} = 4\pi Dr = 1.5^{+0.9}_{-0.6}\,M_\odot$, where we compute r by assuming the shock velocity of 10,000 km s^{-1} (to be consistent with the same calculation by S. Tinyanont et al. 2019). If we use the best-fit radius (3.8×10^{17} cm) from the dust-fitting process, we get $M_{\rm CSM,wind} = 1.9^{+1.1}_{-0.7}\,M_\odot$. The takeaway is that $\sim 2\,M_\odot$ of the CSM has been processed by the shock.

3.3. Dust Location and Origin

While the blackbody radius can constrain the location of the dust, we show here that it may not be sufficient to discriminate between different dust origins. The blackbody radius is usually computed by assuming that the observed dust luminosity and temperature come from blackbody radiation. Here, $r_{\rm bb} = \sqrt{L/4\pi\sigma_{\rm SB}T^4}$, where $\sigma_{\rm SB}$ is the Stefan–Boltzmann constant. If the dust cloud is optically thin in the IR, then $r_{\rm bb}$ is the lower limit of the dust location; if the IR optical depth is much smaller than 1, $r_{\rm bb}$ is not a constraining lower limit. Moreover, this analysis assumes that the dust distribution is spherically symmetric, which may not be the case in most interacting SNe, including this SN.

We compute the blackbody radius at the JWST epoch, using the total luminosity and the mass-weighted averaged temperature of the dust since we have two dominating components. Using this temperature only affects the final radius by less than a percent. The computed blackbody radius is $r_{\rm BB} = (1.50 \pm 0.02) \times 10^{17}$ cm. This is about half of the current shock radius (3×10^{17} cm), assuming the shock velocity of $v_s = 10{,}000$ km s^{-1}. Figure 4(d) shows the evolution of the blackbody radius inferred from IR observations of SN 2014C.

However, the IR optical depth of the dust emission in SN 2014C has been low at all epochs. For the JWST observation, we already show above that the optical depth is only $\sim$0.15 outside of the strong silicate band. For the Spitzer observations, we calculate the IR optical depth to be $\sim$0.5 at 500 days, decreasing to 0.04 at 1920 days, in the observed bands. Because of the low optical depth, the blackbody radius $r_{\rm bb}$ is much smaller than the dust location $r_{\rm dust}$ at all epochs, and it does not serve as a good indicator of the dust location. The much larger $r_{\rm bb}$ at the JWST epoch is due entirely to the lower temperature.

We instead turn to the dust mass and temperature evolution to discern the dust origin. The dust temperature and mass evolution (Figures 4(a) and (b)) are relatively flat in the range 500–2000 days, even at the epoch including observations around 10 μm. S. Tinyanont et al. (2019) conclude that the observed dust is preexisting in the CSM, getting heated by the

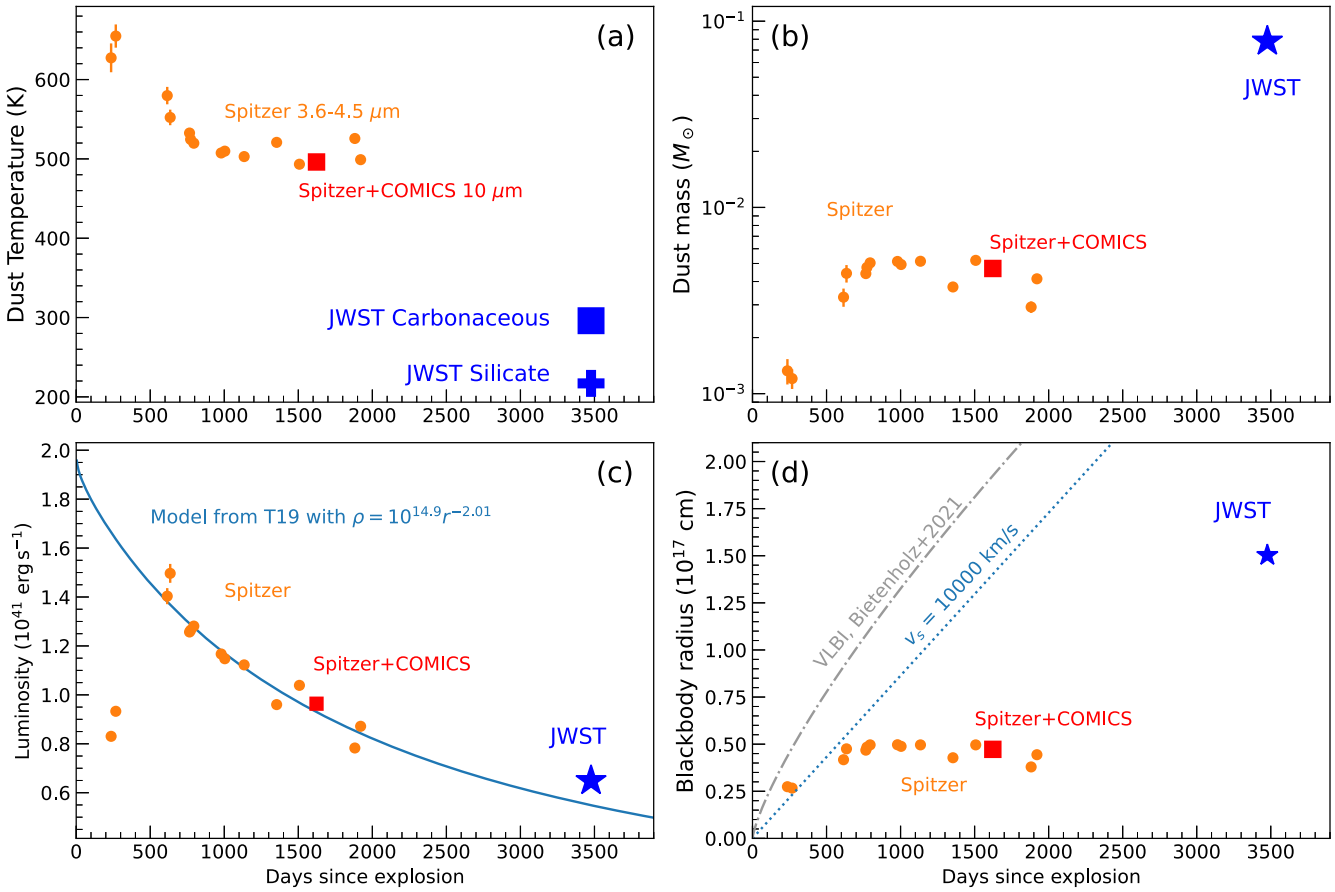

Figure 4. (a) Dust-temperature evolution of SN 2014C. Orange points are from Spitzer 3.6 to 4.5 μm observations, and the red point is from Spitzer plus a ground-based 9.7 μm image from S. Tinyanont et al. (2019). These measurements are photometric, and the dust models have a mixture of carbonaceous and silicate dust at a single temperature. The mass ratio is fixed by the observations including the 10 μm point. The blue square and plus sign are the carbonaceous and the silicate dust components observed by JWST. (b) Dust mass evolution, showing an order of magnitude jump from $\sim 5 \times 10^{-3}$ $M_\odot$ during the Spitzer era to 0.078 $M_\odot$ observed by JWST (total of both carbonaceous and silicate dust). We note that this is the minimum mass required to fit the observed SED. (c) Bolometric luminosity. The semianalytic model fit to the Spitzer data is plotted as a cyan line (from S. Tinyanont et al. 2019). The new observation shows that SN 2014C is behaving as expected by the semianalytic model, indicating that the interaction with the same wind-like CSM component is still ongoing. (d) Blackbody radius of the IR emission. Two estimates of the shock location are provided: one derived from the VLBI measurement (M. F. Bietenholz et al. 2021), and one with a constant velocity of 10,000 km s^{-1}. We note that error bars are plotted for all points, but are smaller than the marker in some cases.

interaction front. This is because the CSM has a wind-like density profile $\rho \propto r^{-2}$ (inferred from light-curve fitting), and the outgoing shock has a surface area growing as $A \propto r^2$. Thus, the mass of CSM dust being heated by the shock is roughly constant, assuming that shock heats the CSM dust out to some distance in front of it.

We do caution that caveats applied for previous observations with minimal mid-IR coverage. At epochs between 1620 and 1900 days, there are only observations in the Spitzer 3.6 and 4.5 μm bands, which are insensitive to further cooling, and the dust could be cooling and increasing during this time. The SED fit to the Spitzer and ground-based mid-IR photometry from $\sim$1620 days presented in S. Tinyanont et al. (2019) is not unique, and cannot rule out a more massive dust component ($\sim$0.03 $M_\odot$) at $\sim$ 250 K. The fit simply used the least amount of dust to explain the observed SED. Using a more massive and cooler component to explain the 10 μm flux does not result in a better fit. In addition, we do not expect cold, newly formed dust, in addition to the observed $\sim$500 K dust at this phase. Ejecta dust would have created red-wing suppression of optical lines that we do not observe (Section 4). There could be new dust in the cold dense shell (CDS) between the forward and reverse shocks at this phase, but it should not be colder than what we later observed with JWST as the interaction flux was higher at 1620 days. A detailed hydrodynamical simulation would be required to predict the dust temperature evolution.

The JWST observations at 3477 days show that the minimum dust mass required to fit the spectrum has increased by an order of magnitude, while the temperature plummets by half. As a sanity check, we perform a dust fitting on synthetic photometry in the same photometric bands (K_s, L, M, Spitzer 3.6 and 4.5 μm, and Subaru/COMICS N9.7, N10.5, and N11.7) using the JWST spectrum, and also find a large increase in dust mass. Therefore, this mass increase is not due to the increased wavelength coverage of the JWST data. We also know from the luminosity evolution (Figure 4(c)) that the CSM profile is likely smooth between the Spitzer and JWST observations, so the increase in the observed dust mass cannot be explained by an additional dense CSM component.

The most likely scenario that explains this observation is that new dust has formed in the CDS between the forward and reverse shocks (M. Pozzo et al 2004; N. Smith et al. 2008; N. N. Chugai 2009, 2018; A. Sarangi 2022). At this epoch, there is now enough CSM ($\sim$1.5 $M_\odot$ from Section 3.2) and SN ejecta (a few $M_\odot$, typical for SNe Ib; J. D. Lyman et al. 2016) processed by the forward and reverse shocks. The few $M_\odot$ of

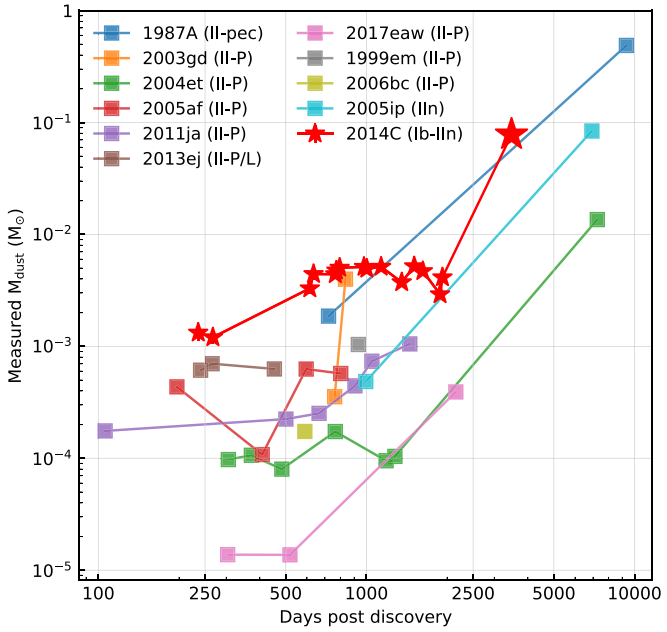

Figure 5. The evolution of the observed dust mass in SN 2014C compared with select CCSNe. These comparison objects are from M. Shahbandeh et al. (2024) and references therein.

material in the CDS is sufficient to condense the observed amount of dust (0.078 $M_\odot$) at a plausible gas-to-dust mass ratio. The newly formed dust has lower temperatures likely due to the higher density of the CDS shielding it from the interaction flux.

Dust formation in the CDS is also consistent with the lack of red-wing absorption observed in the optical lines originating from the reverse shock (Section 4). This is because the CDS dust would be totally outside of the line-emitting region, absorbing both redshifted and blueshifted parts of the line equally. Dust inside the ejecta, on the other hand, would preferentially absorb the redshifted part of emission lines formed outside, which is the case for all spectral lines seen in SN 2014C at this epoch, as we discuss in the next section.

Figure 5 compares the observed dust mass evolution of SN 2014C to those in the literature, including the recent late-time observations of SNe II-P 2004et and 2017eaw (M. Shahbandeh et al. 2023) and SN 2005ip (M. Shahbandeh et al. 2024). The plot shows that the dust mass in SN 2014C evolves in the same manner as that in other CCSNe. We note that, until recently, there were few mid-IR measurements for SNe at early time, and the cold dust mass, missed by these observations, could be significantly higher than what was observed. A sample of CCSNe with JWST observations throughout their evolution is crucial to determine whether this is the case.

4. Spectral Lines Evolution

Optical to IR spectra of SN 2014C continue to be rich in features at the most current epoch, more than 10 yr postexplosion (Figure 3). In addition to our new observations at 3121, 3230, and 3789 day postexplosion, we analyze the Keck/DEIMOS spectrum from 269 days and Keck/LRIS spectrum from 617 days published by J. C. Mauerhan et al. (2018), as well as optical spectra presented by B. P. Thomas et al. (2022). The latest optical spectrum at 3789 days is dominated by strong Hα along with forbidden oxygen lines. High-ionization iron lines such as [Fe VII] λ6087 and [Fe XI] λ7892 disappear before our new observations, as expected by weakening CSM interactions. The last ground-based NIR spectrum shows a clear detection of only the He I 1.083 μm line (shown in Figure 6). Finally, the MIRI MRS spectrum exhibits a strong [Ne II] 12.813 μm line. Owing to the strong galaxy background, reliable flux calibration of the optical lines is not possible given the lack of reliable photometry. The only line for which we have absolute flux calibration is [Ne II] 12.813 μm. These emission lines demonstrate different profiles, indicative of the geometry of their respective formation regions.

4.1. Hα from the CSM

The only hydrogen line left detectable with an intermediate-width ($\sim$1000 km s^{-1}) component at late times is Hα. The progenitor star of SN 2014C is hydrogen poor, so all hydrogen emission comes from the CSM. We fit narrow and broad components to the Hα line simultaneously with the [N II] $\lambda\lambda$6548, 6583 from the host. As also measured by B. P. Thomas et al. (2022), the FWHM of the broad Hα is $\sim$1000 km s^{-1} at all epochs. This is much lower than the FWHM observed in other lines, as the CSM never gets accelerated to the ejecta velocity. We interpret this as the velocity of the shocked CSM in the CDS between the forward and reverse shocks.

4.2. He I 1.083 and 2.059 μm Lines

The He I 1.083 and 2.059 μm lines have been observed at 1354 and 1693 days postexplosion, and only the 2.059 μm line at 275 days, at high S/N by S. Tinyanont et al. (2019). In the new observation at 3807 days, only the stronger 1.083 μm line is clearly detected. Figure 6 (top) shows these lines, in addition to He I λ5876 in comparison with [O III]. We use this oxygen line because it is the only line that persists throughout all phases for which we have NIR observations.

In Figure 6 (middle), we compare line profiles of the NIR helium lines. The line profiles of He I 1.083 and 2.059 μm are broadly similar over the first two epochs; they can be fit with one broad Gaussian (FWHM $\approx$ 4500 km s^{-1}) and two intermediate-width Gaussians (FWHM $\approx$ 1700 km s^{-1}) at around $-$4000 and 0 km s^{-1} (S. Tinyanont et al. 2019), in addition to unresolved narrow components likely from the host galaxy.[36] To be consistent with S. Tinyanont et al. (2019), we refer to these components as "a," "b," and "c," respectively.

Figure 6 (middle) shows Gaussian fits to the He I 1.083 μm line. The broad component "a" has a mean velocity close to zero at all epochs. The FWHM evolves from 8700 to 5900 km s^{-1}. The velocity and its evolution are consistent with this component arising from the SN ejecta heated by the reverse shock. The decreasing velocity corresponds to the reverse shock propagating deeper into the lower-velocity part of the ejecta.

At the first epoch, the centered intermediate-width "c" component is significantly redshifted by 470 and 840 km s^{-1} in the He I 1.083 and 2.059 μm lines, respectively. The similar redshifted feature is seen in the [O III] line at the same epoch as well (Figure 6, top; data from B. P. Thomas et al. 2022). The "c" component of the 1.083 μm line is close to $v = 0$ by 1695 days, while the 2.059 μm line is still significantly redshifted. As such,

[36] S. Tinyanont et al. (2019) reported the standard deviation of the Gaussian, but erroneously marked it as FWHM.

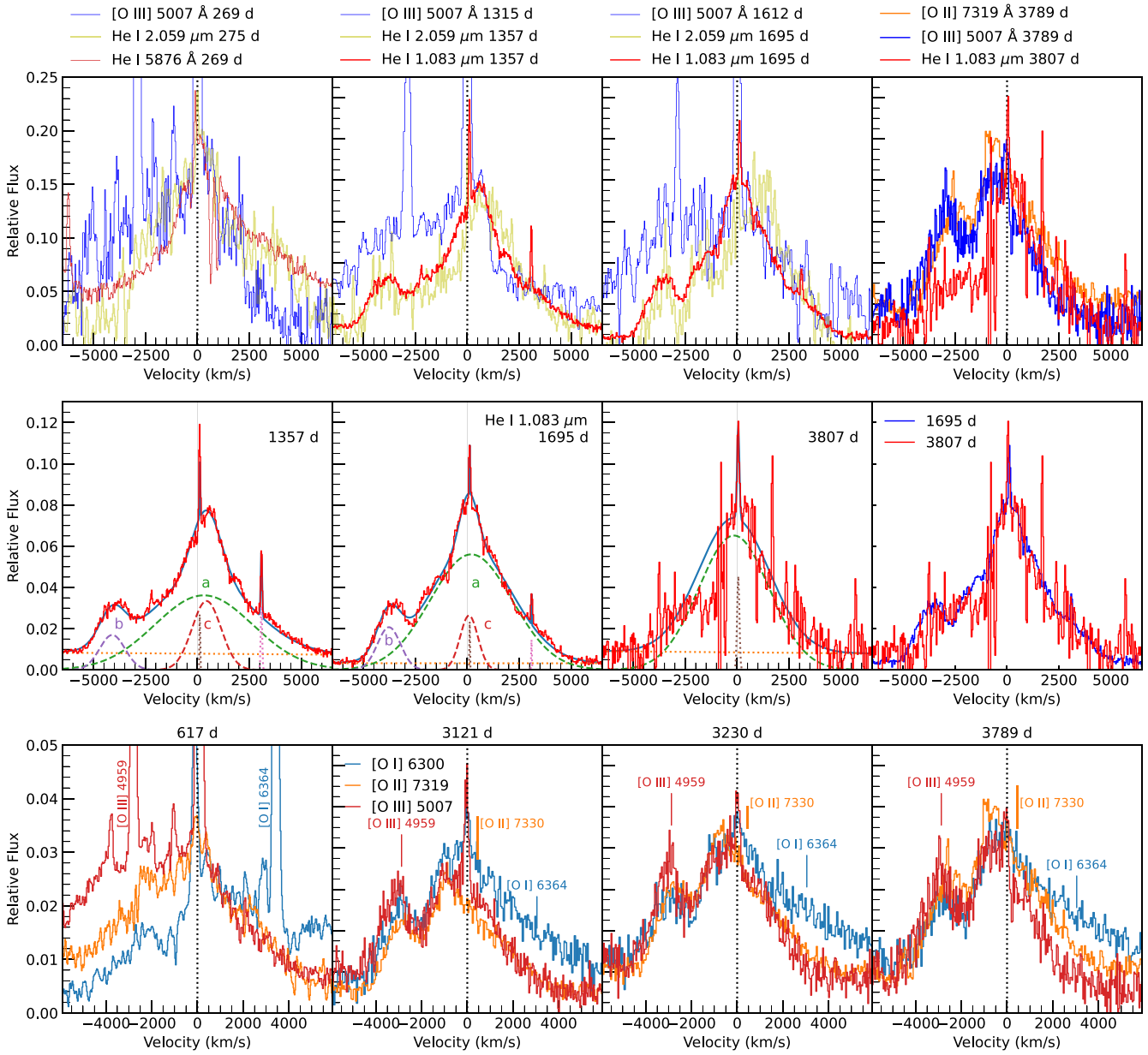

Figure 6. Top: comparisons between the He I 5876 Å, 1.083 μm, and 2.059 μm lines, as well as [O III] 5007 Å at around 270, 1300, 1650, and 3800 days postexplosion. The optical spectrum at 269 day showing He I λ5876 and [O III] is from J. C. Mauerhan et al. (2018). The optical spectra at 1315 and 1612 days showing [O III] are from B. P. Thomas et al. (2022). The NIR spectra from 275, 1357, and 1695 days showing helium lines are from S. Tinyanont et al. (2019). Middle: model fit to the He I 1.083 μm line profile shown in the top panel. The 1357 and 1695 day epochs are presented by S. Tinyanont et al. (2019). They can be fit with a broad component ("a") likely from the ejecta, and two intermediate-width components likely from the CDS. Component "b" is blueshifted to about -4000 km s^{-1}, while "c" is at rest. The 3807 day epoch can be fitted with one broad Gaussian with some flux absorbed around -1800 km s^{-1}. The rightmost panel compares the profile of the 1.083 μm line at 1695 and 3807 days to highlight the potential switch of the blueshifted component from emission to absorption. Bottom: comparisons between forbidden oxygen doublets [O I], [O II], and [O III] at 617, 3121, 3230, and 3789 days. The first-epoch spectrum is from J. C. Mauerhan et al. (2018). The spectral profiles of the three lines are similar in the last two epochs, and only evolve slightly between those epochs.

this component is likely from the ejecta that pass through the reverse shock into the CDS.

Lastly, there is a blueshifted intermediate-width component "b" centered at around -4000 km s^{-1}. This component is intrinsic to the helium lines, as it is present in both He I 1.083 and 2.059 μm. Like the "c" component, its FWHM remains relatively constant at 1200 km s^{-1}. The velocity of the line center of this blueshifted component evolves from -4100 to -3800 km s^{-1} over the first two epochs.

In the last epoch at day 3807, this component turned into absorption (see Figure 6, middle right), and the line profile can be interpreted as a broad Gaussian getting absorbed in the blueshifted part, around -1800 km s^{-1}. This indicates that the reverse shock has passed through the helium-rich part of the asymmetric ejecta responsible for the blueshifted component, and is now illuminating the part approaching the observer from behind.

The lack of a companion redshifted component could be due to dust obscuring the receding part of the ejecta responsible for component "b"; however, we argue that this is not the case. As discussed earlier in Section 3.1, the dust in SN 2014C has grown in mass by an order of magnitude between 2000 and

3500 days postexplosion, but the helium line profile has not evolved significantly. Lastly, [Ne II] 12.813 μm, which we will later discuss, shows a profile very similar to that of the optical lines, despite dust having very small opacity at that wavelength compared with at 1 μm.

4.3. Forbidden Oxygen Lines

Forbidden oxygen lines are prominent in the latest optical spectrum at 3789 days; we identify the [O I] $\lambda\lambda$6300, 6364, [O II] $\lambda\lambda$7319, 7330, and [O III] $\lambda\lambda$4959, 5007 doublets. The feature at $\sim$7319 Å was identified as [Ca II] $\lambda\lambda$7291, 7324 by B. P. Thomas et al. (2022). We disfavor this identification because the two relatively widely spaced [Ca II] doublets are equally strong and should lead to a broader line profile. The profile we observe for this feature is more similar to that of [O I] and [O III], when centered around the stronger [O II] λ7319 line. Further, the two lines that are more likely [Ca II] are present in the spectrum at 269 days, along with the Ca II NIR triplet. These features faded by 617 days. Indeed, similar arguments were made in favor of [O II] over [Ca II] in late-time spectra of SN 1980K (R. A. Fesen et al. 1999). Figure 6 (bottom) compares the line profiles of the forbidden oxygen lines at three epochs postexplosion.

The [O I] and [O III] doublets show a strong, narrow component in the 617 day spectrum from the unshocked CSM heated by the interaction flux (this component is much brighter than the host emission at this epoch). It gets weaker with time relative to the underlying broad component. We agree with the interpretation of B. P. Thomas et al. (2022) that the broad component of forbidden lines arises from the SN ejecta heated by the reverse shock based on their higher velocity compared with the Hα line, and the velocity similar to that of the broad helium lines.

In addition to the forbidden oxygen lines, we note that [S III] λ9531 is detected between 3121 and 3789 days. Its line profile is similar to that of oxygen. This line was outside of the spectral coverage in the B. P. Thomas et al. (2022) data set.

Most notably, the forbidden oxygen lines all show a blueshifted component at around $-3000\,\mathrm{km\,s^{-1}}$, very similar to what is observed in the helium lines. At 1300 and 1650 days, the blueshifted component in the oxygen line is still not obvious (Figure 6, top), but this feature becomes strong by day 3121 (Figure 6, bottom). Because these forbidden lines are optically thin, their profile reflects the gas distribution. The similarity in the line profile across multiple species at different wavelengths suggests that this feature is due to the asymmetry in the common line-forming region, likely the CDS, for these intermediate-width lines.

4.4. [Ne II] 12.813 μm and [Ne III] 15.550 μm

The only strongly detected line from the JWST/MRS data that has a broad component is [Ne II] 12.813 μm. The [Ne III] 15.550 μm line is marginally detected. Figure 7 shows these two lines in velocity space.

Figure 1 (top) demonstrates that there are several star-forming knots in the host galaxy that are luminous in [Ne II] 12.813 μm. However, the flux presented here, especially the broad component, is from the SN. We note that the broad component seen under the [Ne II] line in the background spectrum in Figure 1 (bottom) is from the underlying PAH feature at 12.7 μm, and its subtraction residual does not significantly affect the broad component of the [Ne II] 12.813 μm line from the SN. This line has recently gained attention as the primary coolant for systems with magnetar heating (L. Dessart 2024). Forbidden oxygen lines are also a significant coolant in those systems, and have been used as evidence for a pulsar wind nebula in SN 2012au (D. Milisavljevic et al. 2018). The presence of these lines in SN 2014C, along with Hα, suggests that CSM interaction can also excite these forbidden lines, complicating the interpretation. In addition, we note that forbidden oxygen and mid-IR neon (and other forbidden) lines are also present in SN remnants (e.g., T. Kravtsov et al. 2024; D. Milisavljevic et al. 2024).

The [Ne II] line in SN 2014C has a generally similar profile to that of the forbidden oxygen lines. Because the dust optical depths at 0.7 and 12.8 μm differ by 2 orders of magnitude, the line profile must be intrinsic to the geometric distribution of gas and not due to preferential dust absorption. The profile can be fitted with a narrow, unresolved, Gaussian component at rest

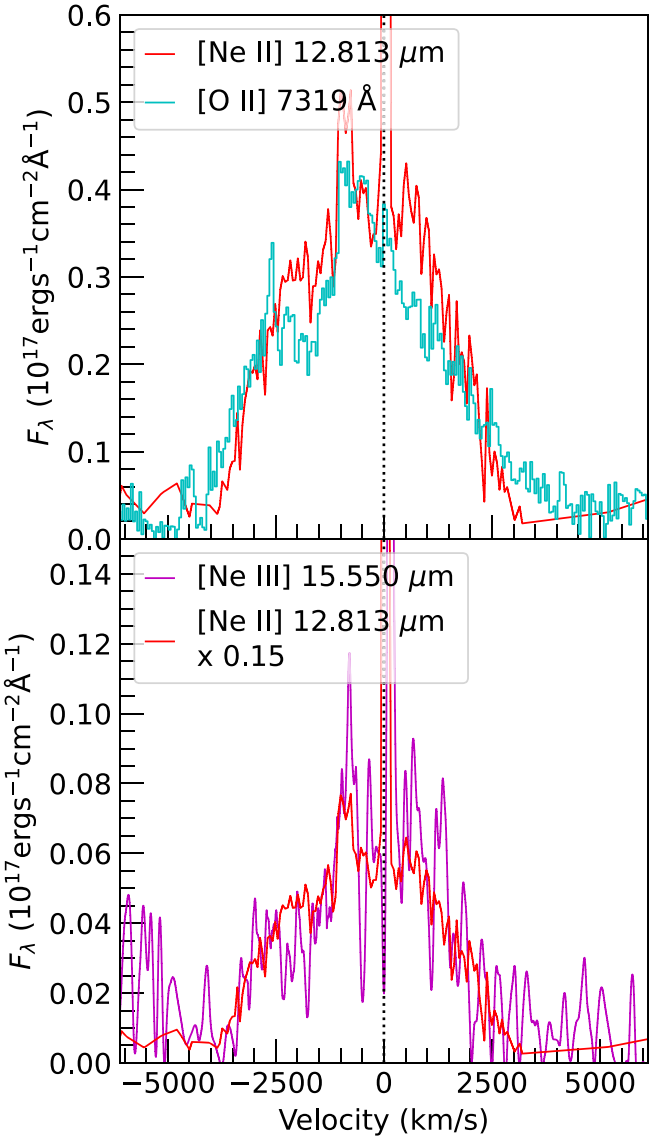

Figure 7. MIRI MRS spectrum showing [Ne II] 12.813 μm (top) and [Ne III] 15.550 μm (bottom). The absolute flux is provided in F_λ, and the dust continuum has been subtracted. In the top panel, the scaled line profile of [O II] λ7319 from day 3789 is provided for comparison. In the bottom panel, [Ne II] 12.813 μm scaled by a factor of 0.15 is shown for comparison.

and a broad Gaussian (FWHM $=4500\,\mathrm{km\,s^{-1}}$) centered at $-440\,\mathrm{km\,s^{-1}}$. The blueshifted intermediate-width component is less pronounced in this line.

With absolute flux calibration, we can use this line to constrain the location of the emission region. We integrate the line luminosity of the broad component, excluding the narrow component that could be from host contamination. The line luminosity in the broad component is $L_{[\mathrm{Ne\ II}]} = (2.4 \pm 0.1) \times 10^{38}\,\mathrm{erg\,s^{-1}}$. For an optically thin line, the luminosity is a volume integral

$$L = \int 4\pi j_{ki}\, dV = \int n_k A_{ki} h\nu_{ki}\, dV, \tag{4}$$

where j_{ki} is the emission coefficient of this transition, n_k is the number density of the ions in the upper state, A_{ki} is the Einstein A coefficient, h is the Planck constant, and ν_{ki} is the frequency of this line. If we assume a constant-density shell of emission with inner and outer radii R_i and R_o, we get

$$L = \frac{4}{3}\pi n_k A_{ki} h\nu_{ki}(R_o^3 - R_i^3). \tag{5}$$

The Einstein A coefficient of this line is $A_{21} = 8.59 \times 10^{-3}\,\mathrm{s^{-1}}$. The density range where we expect to see forbidden lines is 10^3–$10^5\,\mathrm{cm^{-3}}$. With the lower-density end at $n = 10^3\,\mathrm{cm^{-3}}$, $(R_o^3 - R_i^3) = 4.3 \times 10^{49}$ cm^3. If we assume that the emission region is a filled sphere with $R_i = 0$, the radius is $R_o = 3.5 \times 10^{16}\,\mathrm{cm}$. Coincidentally, this is roughly the same as the radius of the CSM-free inner bubble determined from the time delay to the onset of interaction (R. Margutti et al. 2017). If we assume that the emission region is a shell with $R_i > 0$, the shell becomes thin very quickly. With $R_i = 2.6 \times 10^{16}\,\mathrm{cm}$, the fractional thickness of the shell is already $(R_o - R_i)/R_i = 0.5$. Such thin shells would produce a flat-topped or double-peaked line profile, inconsistent with our observations. As such, our data suggest that the [Ne II] 12.813 μm line originates primarily from the SN ejecta, heated at this epoch by the offset CSM, resulting in the overall blueshift of the broad component. The lack of an intermediate component indicates that the reverse shock has not significantly processed the Ne-rich part of the ejecta yet.

Lastly, we note that we do not detect other mid-IR lines predicted by L. Dessart (2024) with an intermediate-width component. Specifically, we checked the [Ni II] 6.634, [Ar II] 6.983, [Ni III] 7.347, and [Ar III] 8.989, and [S III] 18.708 μm lines, and only detect narrow emission from the host in most cases.

4.5. Ejecta and CSM Geometry Constrained by Emission Lines

The consistent profile across many optically thin forbidden lines and the helium lines point to the complicated CSM geometry of SN 2014C. Given the size constraint and the relatively symmetric line profile, we argue that [Ne II] 12.813 μm originates from the inner ejecta, heated by emission from the reverse shock. Because of the similarity in the line profile, the broad component of helium and forbidden oxygen lines likely come from the inner ejecta. The decreasing FHWM velocity of this component observed most clearly in the helium lines supports this interpretation, as the reverse shock traverses to the inner ejecta with lower velocity.

The mean velocity evolution observed in several lines points to a CSM distribution in which its center is slightly offset from the SN location. First, at 1357 days, the broad and intermediate-width (from the CDS) components of the helium lines are redshifted by around $400\,\mathrm{km\,s^{-1}}$. A similar shift is also seen in the [O III] line at a comparable epoch (Figure 6, top). This could be explained if the CSM is closer to the SN on the side away from us; the SN shock interacts with that part of the CSM more strongly at early times, producing redshifted helium lines and the ledge feature seen in [O III] at similar epochs. We note that, while likely originating from a merger (e.g., T. Morris & P. Podsiadlowski 2007), the equatorial CSM ring around SN 1987A is also offset from the SN, with the shock interaction starting on the northeast portion of the ring in 1995 (G. Sonneborn et al. 1998; S. S. Lawrence et al. 2000). G. Sonneborn et al. (1998) also reported blueshifted Hα emission without an associated redshifted component, which they attributed to an interaction with an inward protrusion of the CSM ring.

The CSM on the side away from the observer is overcome sooner, and by 3121 days, the interaction is dominated by the CSM on the side closer to us. This leads to the significant mean velocity of $-440\,\mathrm{km\,s^{-1}}$ observed in the [Ne II] line, which suggests that the reverse shock (which is the power source) is stronger in the part of the ejecta approaching the observer at this phase. The enhanced CSM in the side closer to us also leads to the blueshifted intermediate-width component observed in the forbidden oxygen lines at around $-3000\,\mathrm{km\,s^{-1}}$, and the blueshifted broad component of [Ne II]. At this epoch, the reverse shock has likely passed through the helium-rich part of the ejecta. As a result, the blueshifted helium emission appears in absorption by 3807 days postexplosion (Figure 6, middle).

The prolonged presence of the blueshifted intermediate-width component in optically thick lines points to an asymmetric distribution of material confined to a small range of ejecta velocity in the SN. In the long-lasting SN IIn KISS15s, M. Kokubo et al. (2019) reported a similar line profile in Hα, and they associated it with a plume of high-velocity ejecta expanding through a low-density region in the CSM. A similar picture could be the case for SN 2014C, but with hydrogen-poor, helium-rich ejecta, so this feature only appears in helium and forbidden metal lines, not hydrogen. If this is the case, then the CSM has to take up more of the solid angle around the SN than a disk previously proposed in the literature. Because there is no redshifted component even when the dust optical depth is low, it is unlikely that there is an opposite plume hidden from view.

5. Conclusion

SN 2014C remains an explosion in action for more than a decade. Optical and IR spectra still show emission lines excited by the ongoing interactions. Persistent Hα at $\sim$1000 km s^{-1} demonstrates that the interaction with hydrogen-rich CSM is still ongoing, and this line emerges from the shocked CSM. Forbidden oxygen lines in the optical, helium lines in the NIR, and a forbidden neon line in the mid-IR reveal a complex geometry of the CSM. They all have a broader-width component $\sim$5000 km s^{-1}, likely excited by the reverse shock propagating back into the ejecta. They also show an intermediate-width $\sim$1000 km s^{-1} component from the slower CDS. The helium and oxygen lines exhibit an additional blueshifted intermediate-width component, centered at around $-4000\,\mathrm{km\,s^{-1}}$, that could be from an ejecta plume pointing toward the observer. This component of the helium line turns

from emission into absorption, which is expected in this scenario as the reverse shock traverses the helium-rich part of the ejecta.

Our JWST NIRSpec and MIRI observations capture the bulk of the bolometric luminosity, and show that SN 2014C is still following a decline predicted by a semianalytic model of CSM interaction fit to the Spitzer data by S. Tinyanont et al. (2019). From that model, the CSM is wind-like with $\rho \propto r^{-2}$, but need not be isotropic. The shock is at a radius of $\sim 3 \times 10^{17}$ cm at the time of the JWST observations, and has interacted with at least 1.6 $M_\odot$ of CSM.

Fitting the mid-IR continuum, we find that 0.0780 $M_\odot$ of dust at ∼245 K has formed, likely in the CDS between the forward and reverse shocks. This dust mass increases by a factor of ∼10 from the last observations around days 1600–2200, for which we have mid-IR imaging from the ground. A dust optical depth analysis shows that the dust is likely optically thin, and the mass observed reflects the true mass of the dust at temperatures detectable with MIRI. This is among the highest dust mass in an SN observed around this epoch. Along with recent JWST observations of SNe IIn (e.g., SN 2005ip, M. Shahbandeh et al. 2024), and upcoming results from the GO-1860 (PI Fox) program, we find that interacting SNe produce significantly more dust than noninteracting objects. The relative rate of interacting SNe in the early Universe must be better modeled to accurately account for the dust observed in nascent galaxies.

Acknowledgments

Part of this research benefited from the JWST Data Analysis and Processing Workshop (South East Asia), organized by the National Astronomical Research Institute of Thailand (NARIT) in 2024 July with support from the IAU Hands-On-Workshops and COSPAR Capacity Building programs. S.T. thanks N. Leethochawalit and K. Chanchaiworawit for leading the organization effort, and J. Alvarez Marquez for his instruction on NIRSpec IFU and MIRI MRS data reduction. He also thanks T. Moriya and C. Fransson for useful discussions.

This work is based in part on observations made with the NASA/ESA/CSA James Webb Space Telescope. The data were obtained from the Mikulski Archive for Space Telescopes at the Space Telescope Science Institute, which is operated by the Association of Universities for Research in Astronomy, Inc., under NASA contract NAS 5-03127 for JWST. These observations are associated with program GO-2348. This work was supported by National Aeronautics and Space Administration (NASA) Keck PI Data Awards, administered by the NASA Exoplanet Science Institute. S.T. and K.W. acknowledge support by the Fundamental Fund of Thailand Science Research and Innovation (TSRI) grant FFB680072/0269 through NARIT. K.M. acknowledges support from JSPS KAKENHI grants JP24H01810 and 24KK0070. The UCSC team is supported in part by STScI grants JWST-GO-2348, JWST-DD-6659, and JWST-DD-6838; NASA grants 80NSSC23K0301 and 80NSSC24K1411; and a fellowship from the David and Lucile Packard Foundation to R.J.F. Financial support to L.G. is acknowledged from the Spanish Ministerio de Ciencia, Innovación y Universidades (MCIU) and the Agencia Estatal de Investigación (AEI) 10.13039/501100011033 under the PID2020-115253GA-I00 HOSTFLOWS and PID2023-151307NB-I00 SNNEXT projects, from Centro Superior de Investigaciones Cientìficas (CSIC) under the projects PIE 20215AT016, ILINK23001, COOPB2304, the program Unidad de Excelencia Marìa de Maeztu CEX2020-001058-M, and from the Departament de Recerca i Universitats de la Generalitat de Catalunya through the 2021-SGR-01270 grant. A.V.F.'s group at UC Berkeley has received financial assistance from the Christopher R. Redlich Fund, Gary and Cynthia Bengier, Clark and Sharon Winslow, Alan Eustace (W.Z. is a Bengier–Winslow–Eustace Specialist in Astronomy), William Draper, Timothy and Melissa Draper, Briggs and Kathleen Wood, Sanford Robertson (T.G.B. is a Draper–Wood–Robertson Specialist in Astronomy; Y.Y. was a Bengier-Winslow-Robertson Fellow in Astronomy), and numerous other donors. Z.G.L. is supported by the Marsden Fund administered by the Royal Society of New Zealand, Te Apārangi under grant M1255. C.L. acknowledges support under DOE award DE-SC0010008 to Rutgers University. D.M. acknowledges support from the National Science Foundation (NSF) through grants PHY-2209451 and AST-2206532. J.R. acknowledges financial support from a NASA ADAP grant (80NSSC23K0749). T.T. acknowledges support from the NSF grant AST-2205314 and NASA ADAP award 80NSSC23K1130. Q.W. is supported by the Sagol Weizmann-MIT Bridge Program.

Part of this work uses the Chalawan High-Performance Computer Cluster at NARIT. Some of the data presented in this paper were obtained from the Mikulski Archive for Space Telescopes (MAST). STScI is operated by the Association of Universities for Research in Astronomy, Inc., under NASA contract NAS5-26555. Support for MAST for non-HST data is provided by the NASA Office of Space Science via grant NNX13AC07G and by other grants and contracts. Some of the data presented herein were obtained at Keck Observatory, which is a private 501(c)3 nonprofit organization operated as a scientific partnership among the California Institute of Technology, the University of California, and NASA. The Observatory was made possible by the generous financial support of the W. M. Keck Foundation. The authors wish to recognize and acknowledge the very significant cultural role and reverence that the summit of Maunakea has always had within the Native Hawaiian community. We are most fortunate to have the opportunity to conduct observations from this mountain. This research has made use of the Keck Observatory Archive (KOA), which is operated by the W. M. Keck Observatory and the NASA Exoplanet Science Institute (NExScI), under contract with NASA.

Appendix
Markov Chain Monte Carlo Sampling of the Dust Parameters

We use the `emcee` package (D. Foreman-Mackey et al. 2013) to perform Markov Chain Monte Carlo sampling of the dust parameters presented in Section 3.1. The free parameters in the fit are the temperature and mass of two carbonaceous dust components and one silicate dust component. The prior distributions are uniform with the allowed ranges $1 \leqslant T \leqslant 3000$ K and $10^{-7} \leqslant M \leqslant 2 M_\odot$. The log likelihood function is $\ln \lambda = -0.5 \sum_\lambda (y_\lambda - m_\lambda)^2 / (\sigma_\lambda^2)$, where y_λ and σ_λ are (respectively) the observed flux and uncertainty at wavelength λ, and m_n is the model flux at that wavelength. We run 32 walkers in 50,000 steps, and use the `get_autocorr_time` function of `emcee` to automatically determine the burn-in steps to remove. The chains converge quickly after around 100 steps, and we remove the first 500 steps from the analysis. Figure A.1 shows the corner plot of the posterior distribution of the fitted parameters.

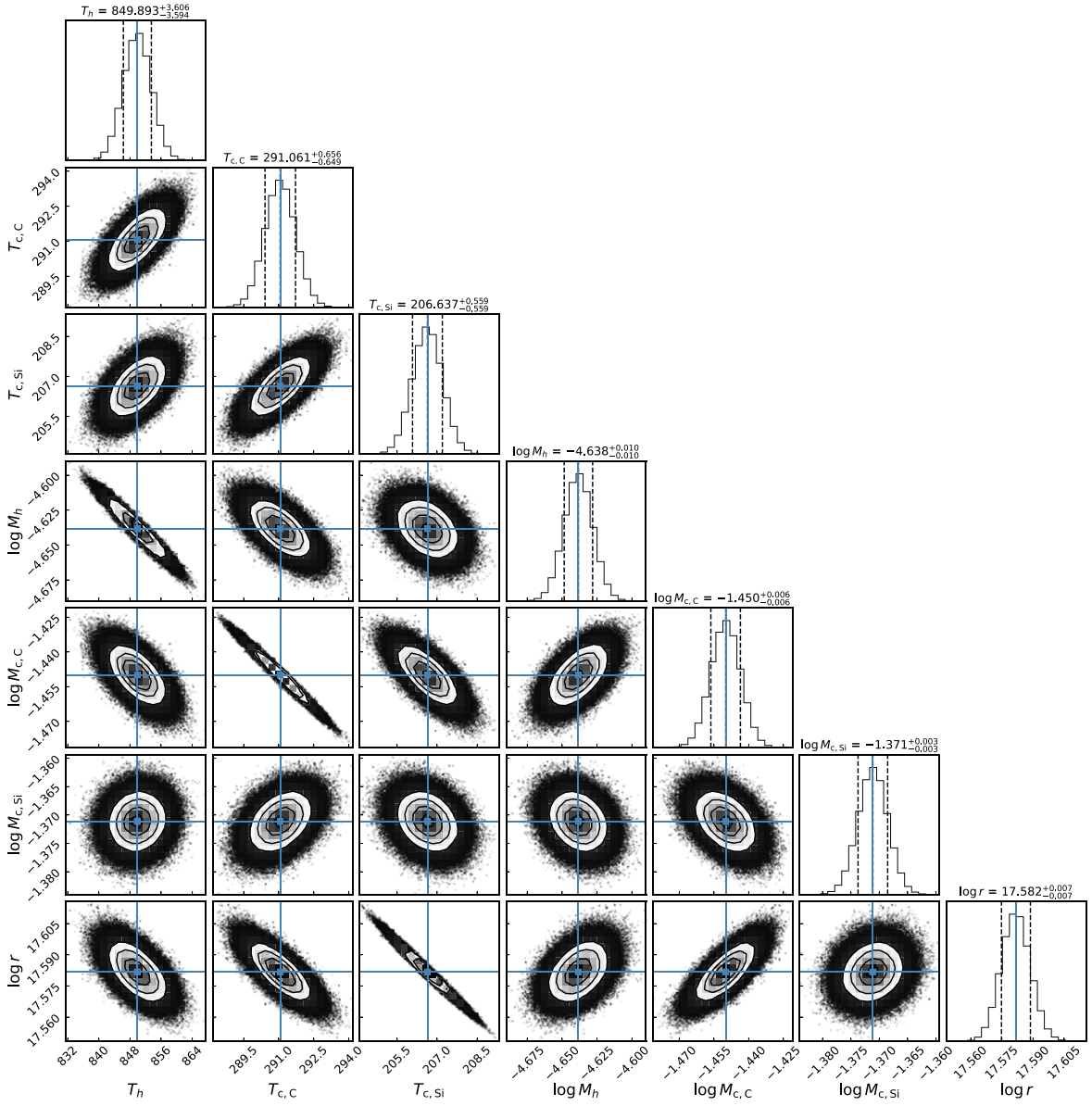

Figure A.1 Corner plot of the posterior distribution of dust-fitting parameters used in modeling the IR spectrum of SN 2014C.

ORCID iDs

Samaporn Tinyanont https://orcid.org/0000-0002-1481-4676
Ori D. Fox https://orcid.org/0000-0003-2238-1572
Melissa Shahbandeh https://orcid.org/0000-0002-9301-5302
Tea Temim https://orcid.org/0000-0001-7380-3144
Robert Williams https://orcid.org/0000-0002-3742-8460
Kittipong Wangnok https://orcid.org/0000-0002-7593-2748
Armin Rest https://orcid.org/0000-0002-4410-5387
Ryan M. Lau https://orcid.org/0000-0003-0778-0321
Keiichi Maeda https://orcid.org/0000-0003-2611-7269
Jacob E. Jencson https://orcid.org/0000-0001-5754-4007
Katie Auchettl https://orcid.org/0000-0002-4449-9152
Alexei V. Filippenko https://orcid.org/0000-0003-3460-0103
Conor Larison https://orcid.org/0000-0003-2037-4619
Chris Ashall https://orcid.org/0000-0002-5221-7557
Thomas G. Brink https://orcid.org/0000-0001-5955-2502
Kyle W. Davis https://orcid.org/0000-0002-5680-4660
Luc Dessart https://orcid.org/0000-0003-0599-8407
Ryan J. Foley https://orcid.org/0000-0002-2445-5275
Lluís Galbany https://orcid.org/0000-0002-1296-6887
Matthew Grayling https://orcid.org/0000-0002-6741-983X
Joel Johansson https://orcid.org/0000-0001-5975-290X
Mansi M. Kasliwal https://orcid.org/0000-0002-5619-4938
Zachary G. Lane https://orcid.org/0009-0003-8380-4003
Natalie LeBaron https://orcid.org/0000-0002-2249-0595
Dan Milisavljevic https://orcid.org/0000-0002-0763-3885
Jeonghee Rho https://orcid.org/0000-0003-3643-839X
Itsuki Sakon https://orcid.org/0000-0001-7641-5497
Arkaprabha Sarangi https://orcid.org/0000-0002-9820-679X
Tamás Szalai https://orcid.org/0000-0003-4610-1117
Kirsty Taggart https://orcid.org/0000-0002-5748-4558
Schuyler D. Van Dyk https://orcid.org/0000-0001-9038-9950
Qinan Wang https://orcid.org/0000-0001-5233-6989
Yi Yang https://orcid.org/0000-0002-6535-8500
WeiKang Zheng https://orcid.org/0000-0002-2636-6508
Szanna Zsíros https://orcid.org/0000-0001-7473-4208

References

Agliozzo, C., Phillips, N., Mehner, A., et al. 2021, A&A, 655, A98
Argyriou, I., Glasse, A., Law, D. R., et al. 2023, A&A, 675, A111
Balasubramanian, A., Corsi, A., Polisensky, E., Clarke, T. E., & Kassim, N. E. 2021, ApJ, 923, 32
Beasor, E. R., & Davies, B. 2018, MNRAS, 475, 55
Beasor, E. R., Davies, B., Smith, N., et al. 2020, MNRAS, 492, 5994
Beasor, E. R., & Smith, N. 2022, ApJ, 933, 41
Bietenholz, M. F., Bartel, N., Kamble, A., et al. 2021, MNRAS, 502, 1694
Bietenholz, M. F., Kamble, A., Margutti, R., Milisavljevic, D., & Soderberg, A. 2018, MNRAS, 475, 1756
Böker, T., Beck, T. L., Birkmann, S. M., et al. 2023, PASP, 135, 038001
Brethauer, D., Margutti, R., Milisavljevic, D., et al. 2022, ApJ, 939, 105
Chandra, P., Chevalier, R. A., Chugai, N., Milisavljevic, D., & Fransson, C. 2020, ApJ, 902, 55
Chugai, N. N., & Chevalier, R. A. 2006, ApJ, 641, 1051
Chugai, N. N. 2009, MNRAS, 400, 866
Chugai, N. N. 2018, MNRAS, 481, 3643
Cohen, M., Walker, R. G., Carter, B., et al. 1999, AJ, 117, 1864
Cox, D. P., & Mathews, W. G. 1969, ApJ, 155, 859
de Jager, C., Nieuwenhuijzen, H., & van der Hucht, K. A. 1988, A&AS, 72, 259
Dessart, L. 2024, A&A, 692, A204
Draine, B. T., & Lee, H. M. 1984, ApJ, 285, 89
Drout, M. R., Götberg, Y., Ludwig, B. A., et al. 2023, Sci, 382, 1287
Drout, M. R., Soderberg, A. M., Gal-Yam, A., et al. 2011, ApJ, 741, 97
Eldridge, J. J., Fraser, M., Smartt, S. J., Maund, J. R., & Crockett, R. M. 2013, MNRAS, 436, 774
Ferrari, L., Folatelli, G., Kuncarayakti, H., et al. 2024, MNRAS, 529, L33
Fesen, R. A., Gerardy, C. L., Filippenko, A. V., et al. 1999, AJ, 117, 725
Filippenko, A. V. 1997, ARA&A, 35, 309
Foreman-Mackey, D., Hogg, D. W., Lang, D., & Goodman, J. 2013, PASP, 125, 306
Fox, O. D., Chevalier, R. A., Dwek, E., et al. 2010, ApJ, 725, 1768
Fox, O. D., Chevalier, R. A., Skrutskie, M. F., et al. 2011, ApJ, 741, 7
Fox, O. D., Filippenko, A. V., Skrutskie, M. F., et al. 2013, AJ, 146, 2
Fox, O. D., Van Dyk, S. D., Williams, B. F., et al. 2022, ApJL, 929, L15
Freedman, W. L., Madore, B. F., Gibson, B. K., et al. 2001, ApJ, 553, 47
Galbany, L., Anderson, J. P., Sánchez, S. F., et al. 2018, ApJ, 855, 107
Gal-Yam, A. 2017, in Handbook of Supernovae, ed. A. W. Alsabti & P. Murdin (Berlin: Springer), 195
Gal-Yam, A., Yaron, O., Pastorello, A., et al. 2021, TNSAN, 76, 1
Gehrz, R. D., Hayward, T. L., Houck, J. R., et al. 1995, ApJ, 439, 417
Jakobsen, P., Ferruit, P., Alves de Oliveira, C., et al. 2022, A&A, 661, A80
Kasliwal, M. M., Bally, J., Masci, F., et al. 2017, ApJ, 839, 88
Kataza, H., Okamoto, Y., Takubo, S., et al. 2000, Proc. SPIE, 4008, 1144
Kilpatrick, C. D., Drout, M. R., Auchettl, K., et al. 2021, MNRAS, 504, 2073
Kim, M., Zheng, W., Li, W., et al. 2014, CBET, 3777, 1
Kokubo, M., Mitsuda, K., Morokuma, T., et al. 2019, ApJ, 872, 135
Kravtsov, T., Anderson, J. P., Kuncarayakti, H., Maeda, K., & Mattila, S. 2024, arXiv:2409.06504
Kuncarayakti, H., Anderson, J. P., Galbany, L., et al. 2018, A&A, 613, A35
Kuncarayakti, H., Sollerman, J., Izzo, L., et al. 2023, A&A, 678, A209
Laor, A., & Draine, B. T. 1993, ApJ, 402, 441
Lawrence, S. S., Sugerman, B. E., Bouchet, P., et al. 2000, ApJL, 537, L123
Lyman, J. D., Bersier, D., James, P. A., et al. 2016, MNRAS, 457, 328
Margutti, R., Kamble, A., Milisavljevic, D., et al. 2017, ApJ, 835, 140
Mauerhan, J., Smith, N., Van Dyk, S. D., et al. 2015, MNRAS, 450, 2551
Mauerhan, J. C., Filippenko, A. V., Zheng, W., et al. 2018, MNRAS, 478, 5050
Milisavljevic, D., Patnaude, D. J., Chevalier, R. A., et al. 2018, ApJL, 864, L36
Milisavljevic, D., Margutti, R., Kamble, A., et al. 2015, ApJ, 815, 120
Milisavljevic, D., Temim, T., De Looze, I., et al. 2024, ApJL, 965, L27
Moriya, T. J., Maeda, K., Taddia, F., et al. 2013, MNRAS, 435, 1520
Morris, T., & Podsiadlowski, P. 2007, Sci, 315, 1103
Myers, C., De, K., Yan, L., et al. 2024, ApJ, 976, 230
Oke, J. B., Cohen, J. G., Carr, M., et al. 1995, PASP, 107, 375
Orlando, S., Greco, E., Hirai, R., et al. 2024, ApJ, 977, 118
Pastorello, A., Mattila, S., Zampieri, L., et al. 2008, MNRAS, 389, 113
Pellegrino, C., Howell, D. A., Terreran, G., et al. 2022, ApJ, 938, 73
Perley, D. A. 2019, PASP, 131, 084503
Podsiadlowski, P., Joss, P. C., & Hsu, J. J. L. 1992, ApJ, 391, 246
Pooley, D., Wheeler, J. C., Vinkó, J., et al. 2019, ApJ, 883, 120
Pozzo, M., Meikle, W. P. S., Fassia, A., et al. 2004, MNRAS, 352, 457
Prochaska, J., Hennawi, J., Westfall, K., et al. 2020a, JOSS, 5, 2308
Prochaska, J. X., Hennawi, J., Cooke, R., et al. 2020b, pypeit/PypeIt: Release v1.0.0, Zenodo, doi:10.5281/zenodo.3743493
Rest, A., Pierel, J., Correnti, M., et al. 2023, The JWST HST Alignment Tool (JHAT), v2, Zenodo, doi:10.5281/zenodo.7892935
Ryder, S. D., Van Dyk, S. D., Fox, O. D., et al. 2018, ApJ, 856, 83
Sana, H., de Mink, S. E., de Koter, A., et al. 2012, Sci, 337, 444
Sarangi, A. 2022, A&A, 668, A57
Schlegel, E. M. 1990, MNRAS, 244, 269
Shahbandeh, M., Fox, O. D., Temim, T., et al. 2024, arXiv:2410.09142
Shahbandeh, M., Sarangi, A., Temim, T., et al. 2023, MNRAS, 523, 6048
Shivvers, I., Modjaz, M., Zheng, W., et al. 2017, PASP, 129, 054201
Smith, N. 2014, ARA&A, 52, 487
Smith, N. 2017, in Handbook of Supernovae, ed. A. W. Alsabti & P. Murdin (Berlin: Springer), 403
Smith, N., Foley, R. J., Bloom, J. S., et al. 2008, ApJ, 686, 485
Smith, N., Gehrz, R. D., Campbell, R., et al. 2011a, MNRAS, 418, 1959
Smith, N., Li, W., Filippenko, A. V., & Chornock, R. 2011b, MNRAS, 412, 1522
Sollerman, J., Fransson, C., Barbarino, C., et al. 2020, A&A, 643, A79
Sonneborn, G., Pun, C. S. J., Kimble, R. A., et al. 1998, ApJL, 492, L139
Sun, N. C., Maund, J. R., & Crowther, P. A. 2020, MNRAS, 497, 5118
Sun, N. C., Maund, J. R., & Crowther, P. A. 2023, MNRAS, 521, 2860
Szalai, T., Zsíros, S., Fox, O. D., Pejcha, O., & Müller, T. 2019, ApJS, 241, 38
Tartaglia, L., Sollerman, J., Barbarino, C., et al. 2021, A&A, 650, A174
Thomas, B. P., Wheeler, J. C., Dwarkadas, V. V., et al. 2022, ApJ, 930, 57
Tinyanont, S., Kasliwal, M. M., Fox, O. D., et al. 2016, ApJ, 833, 231
Tinyanont, S., Lau, R. M., Kasliwal, M. M., et al. 2019, ApJ, 887, 75
Tinyanont, S., Foley, R. J., Taggart, K., et al. 2024, PASP, 136, 014201
Waters, L. B. F. M., Morris, P. W., Voors, R. H. M., Lamers, H. J. G. L. M., & Trams, N. R. 1998, Ap&SS, 255, 179
Wells, M., Pel, J. W., Glasse, A., et al. 2015, PASP, 127, 646
Wilson, J. C., Henderson, C. P., Herter, T. L., et al. 2004, Proc. SPIE, 5492, 1295
Zapartas, E., de Mink, S. E., Van Dyk, S. D., et al. 2017, ApJ, 842, 125
Zenati, Y., Wang, Q., Bobrick, A., et al. 2022, arXiv:2207.07146
Zhai, Q., Zhang, J., Lin, W., et al. 2025, ApJ, 978, 163
Zheng, W., Li, W., Filippenko, A. V., & Cenko, S. B. 2014, ATel, 5721, 1